Analysis and experiments of the thermal–optical performance for a kinematically mounted lens element

Xinfeng Yu,[1,*] Mingyang Ni,[1] Wei Zhang,[1] Yongxin Sui,[1] and Shuo Qin[2]

[1]State Key Laboratory of Applied Optics, Changchun Institute of Optics, Fine Mechanics and Physics, Chinese Academy of Sciences, Changchun 130033, China

[2]Air-force Aviation University, Changchun 130021, China

*Corresponding author: yu_xfeng@126.com

Received 19 March 2014; revised 13 May 2014; accepted 13 May 2014; posted 14 May 2014 (Doc. ID 208508); published 20 June 2014

In order to evaluate the thermal–optical performance of a kinematic mounting applied in lithographic projection lens, the optical surface figure and wavefront changes of the lens element under a certain thermal load are investigated with both experimental and numerical simulation methods. From the experimental and numerical results, the temperature on the edge of the lens element rises up to 22.51°C, and the center of lens is 5.3°C higher. As a result, this thermal nonuniformity leads to a 9.622 nm RMS change of the optical surface figure and 71.905 nm RMS change of the index inhomogeneity, consisting mainly of Z4, Z9, and Z16. Because of the radial flexibility of the supporting legs of the kinematic mounting, aberrations such as pri trefoil and sec trefoil are less than 2% of the total wavefront changes, and other nonaxisymmetric aberrations are negligible. The Zernike coefficient differences between experiments and simulation are less than 2 nm, which supports the correctness of our method. The kinematic mounting shows good thermal adaptability, and the method for evaluation of the thermal–optical characteristics is proved effective.

OCIS codes: (220.0220) Optical design and fabrication; (220.3740) Lithography.
http://dx.doi.org/10.1364/AO.53.004079

1. Introduction

In order to satisfy the demand for large-scale integrated circuit development, higher laser power and off-axis illumination technology are used to increase the productivity and resolution of the projection lens [1]. Thus, thermal aberration induced by lens heating becomes more and more important. As a result of laser absorption, lens heating, which leads to temperature rise and inhomogeneous thermal distribution, results in thermal elastic deformation, refractive index change, and thermal stress [2–4]. Among these three main reasons, refractive index change caused by inhomogeneous thermal distribution is a dominating factor for projection lens performance degeneration [4,5].

To avoid the effects of lens heating, the lens mounting should have an athermal design besides the requirements of eigenfrequency and integrated optical surface deformation [6]. Flexible mounting has been an effective technology to minimize the thermal deformation and stress of optical elements and has been widely used in many optomechanical systems [7–9]. The radial flexibility of the mounting structures allows free expansion of the optical elements and causes less internal stress and surface deformation of the optical elements.

Moreover, many advanced compensation methods have been applied in thermal aberration control of the projection lens. Nikon used infrared aberration control (IAC) technology to compensate uniform

1559-128X/14/184079-06$15.00/0

astigmatism caused by dipole illumination [1]. ASML integrated a FlexWave module in a NA 1.35 immersion to minimize lens aberration under high productivity usage of a scanner [10].

However, the above technologies focus on the system aberration compensation; not too much research has been published on the investigation of the optothermal characteristics of the basic lens cell used in the lithographic projection lens. During the design stage, much consideration must be put on the thermal design of the basic lens cell in order to predict the systematic aberration due to lens heating. This paper focuses on the optomechanical characteristics of the kinematic mounting. First, we introduce the principles of kinematic mounting and the method used to analyze the surface figure and wavefront error (WFE). Then the experiment steps and configuration are shown in detail. Finally, the simulation results are compared to the experiment, and the conclusions are discussed to prove the correctness of the research.

2. Principle of Kinematic Mounting

The kinematic mounting design follows the principle of exact constraints, which means the lens element is constrained exactly with all its six degree of freedom, and no redundant constraints are applied. Therefore, the kinematic mounting has the advantages of precise positioning, good repeatability, and low deformation of the optical surface and has been widely adopted in the field of precise optics and measuring instruments [11–13].

The simplified structure of the kinematic mounting used in this paper is shown in Fig. 1. The lens element is supported and connected to the mounts by three equally circumferential distributed supporting legs. Each supporting leg consists of three spherical flexures, one of which is fixed to the lens element, and the other two are fixed to the mounts. The spherical flexures have rotation flexibilities of the $\theta X/\theta Y/\theta Z$ directions and are totally stiff in the other three translations of the $X/Y/Z$ directions. By this configuration, every supporting leg is flexible in the radial direction and stiff in the axial direction

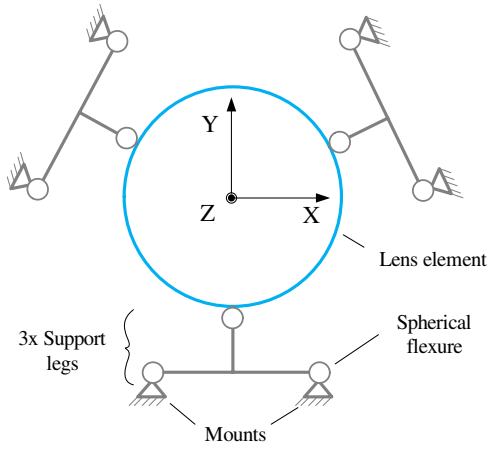

Fig. 1. Schematic diagram of kinematic mounting.

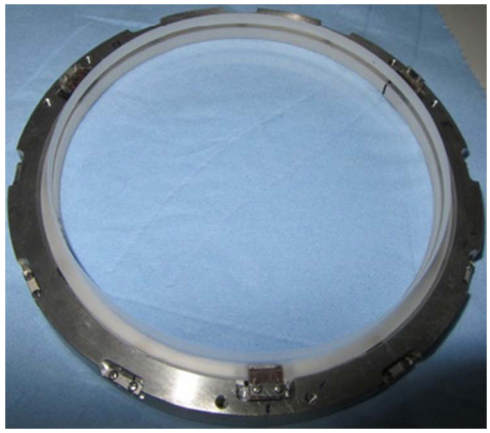

Fig. 2. Element of kinematic mount.

with respect to the lens element. Finally, the exact constraint of the lens element is realized.

Actually, the spherical flexure is connected to the lens element in a contacting manner, forming a relatively better heat conducting path compared to the air gap conduction between the peripheral edge of the lens element and the mount. This may cause uneven thermal distribution within the lens element. Figure 2 shows the integrated assembly of the lens element, supporting legs, and the mount applied in the projection lens.

3. Calculation of Surface Figure and Wavefront

With the assembly of the lens element and mounts, once thermal load and reasonable boundary conditions have been defined, the finite volume method could be used to calculate the temperature distribution. Suppose the normal direction of the optical surfaces for a certain plate is along the Z axis, which is parallel to the propagation direction of the measuring light, the wavefront deviation of the lens element due to thermal load can be expressed as follows:

$$\delta w(x,y) = \int_0^{d_s} (n_0 - 1)\frac{\partial u_z(x,y,z)}{\partial z}\mathrm{d}z + \int_0^{d_s} \frac{\partial n}{\partial T}\delta T(x,y,z)\mathrm{d}z, \quad (1)$$

where $u_z(x,y,z)$ is obtained by the thermal-elastic deformation formula, $\delta T(x,y,z)$ represents the temperature increment between the lens element and the environment, and d_s is the thickness of the lens element. According to Eq. (1), the wavefront deviation consists of two parts. The first term in the right of Eq. (1) is caused by thermal deformation due to the temperature rise of the lens element. This term can be obtained by multiplying $(n_0 - 1)$ with the surface figure deformation of the lens element. The second term represents the effect of index variation of the optical material due to heat absorption. This term cannot be calculated directly unless we have the analytical expression of temperature distribution; thus we transform the integral to summation with use of the temperature data obtained from the finite volume

method. Therefore, the wavefront deviation caused by index variation could be expressed as

$$\int_0^{d_s} \frac{\partial n}{\partial T} \delta T(x,y,z) \mathrm{d}z = \sum_{i=1}^{n} \Delta n_i \Delta L_i, \tag{2}$$

where Δn_i is the index change of every integrated node and ΔL_i is the corresponding integrated length.

In order to give a clear description of the measured and calculated results, wavefront deviations are expanded in terms of Zernike polynomials, which is as follows [14]:

$$z(r,\theta) = \sum_n \sum_m [A_{nm} P_{nm}(\rho) \cos(m\theta) + B_{nm} P_{nm}(\rho) \sin(m\theta)], \tag{3}$$

where

$$P_{nm}(\rho) = \sum_{j=0}^{\frac{n-m}{2}} \frac{(-1)^j (n-j)!}{j! \left(\frac{n+m}{2}-j\right)! \left(\frac{n-m}{2}-j\right)!} \rho^{n-2j}, \tag{4}$$

and $m \le n$, n and m are both odd or even numbers, n is the radial order, m is the azimuth frequency, and ρ is the normalized radius. The Zernike polynomial terms are orthogonal over the unit circle and can reflect the surface deformation individually. In this paper, the fringe Zernike with 37 terms is adopted.

4. Experiments

The lens thickness is 27.38 mm, with a clear aperture of 140.8 mm. As shown in Fig. 3, the experiment configuration consist of a Fizeau phase-shifting interferometer, four FLUKE 5611 temperature sensors and a control box, one piece of film electrical heater and a constant current power supply, and a set of the kinematic mounting assembly. The experiment is carried out in a 1000 class environment control lab, with temperature stability of 22.1 ± 0.05°C. The interferometer uncertainty is 0.4 nm RMS, and the accuracy of the temperature sensor is better than ±0.01°C.

Figure 4 shows the setup of the experiment. The electrical film heater power can be precisely controlled, and hence the thermal load for simulation can be defined. In order to reduce the heat resistance

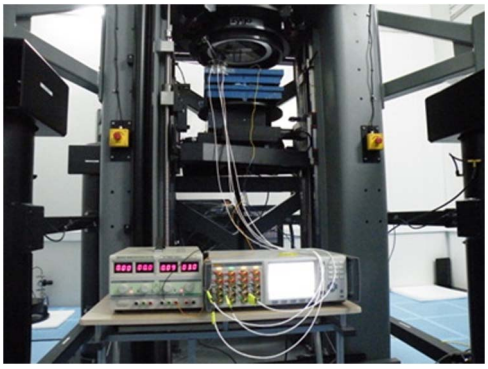

Fig. 3. Experiment system.

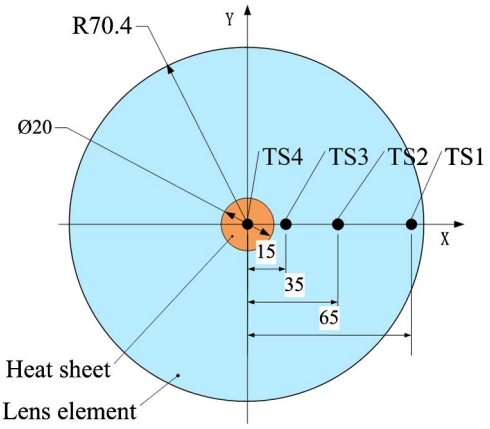

Fig. 4. Configuration of temperature sensors on the film heater.

and measuring error, heat conducting grease is applied between the lens surface and the sensor tips. The film electrical heater is placed in the center of the lens element to generate an axisymmetric thermal load. Four temperature sensors are radially arranged from the center to the edge of the lens element; TS4 records the temperature of the film heater, and TS1, TS2, and TS3 measure the top surface of the lens element. Also the environment temperature is measured to provide boundary conditions for thermal simulation.

The experiment is divided into two steps. The first step is to measure the initial surface figure and wavefront of the lens element before heating; then the specified thermal load will be applied and the surface figure and wavefront measurement will be measured again when the lens element reaches thermal balance. The surface figure change and wavefront deviation due to thermal load will be acquired by subtracting the initial data from the heated data. To reduce the uncertainty of air flow-, vibration-, and heat-caused instability of the interferometer, every effective datum is averaged by 20 measurement points.

5. Experimental and Analytical Simulation Result

A. Boundary Conditions Definition

Figure 5 shows the computation mesh lens element assembly. According to former experiments' results, the convective heat transfer coefficient from the lens element to the environment is set to be 5 W/(m^{2}K), and the contact heat resist between the lens element and the mount is 4000 W/(m^{2}K). Thermal couplings

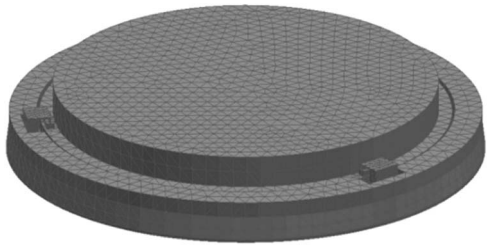

Fig. 5. Computational mesh for lens element.

Table 1. Physical Properties of Materials

Material	Young's modulus/GPa	Poisson's ratio	Thermal expansion coefficient/1/K	Density g/cm^3	Thermal conductivity/W/m/K	$\Delta n/\Delta T$/ppm/K @$\lambda = 632.8$ nm
SiO_2	72.7	0.160	5.80e – 7	2.201	1.3	10.5
Invar 36	141.0	0.259	1.26e – 6	8.050	10.4	—

are applied between the lens element and kinematic mounts based on the conductive path.

The upper surface of the film heater is exposed to the air while the lower surface is in contact with the lens element. Thus the heat absorption of the lens element is given by subtracting environmental heat dissipation from the total power of the film heater, as shown in Eq. (5):

$$\Phi_{\mathrm{h}} = \frac{U^2}{R} - h_f A \Delta T, \tag{5}$$

where U is voltage, R is the electrical resistance of the film heater, h_f is the convective heat transfer coefficient of the top surface of the film heater, A is the heat dissipation area of the film heater, ΔT is the temperature difference between the film heater and the environment, and Φ_h is power absorption of the lens element.

The test result of h_f is 15.019 W/(m^{2}K), V is 3.1 V, R is 32 Ω, and the TS4 indicates 31.6702°C; thus the calculated lens element power absorption is 0.255 W. Physical properties of the optical and mechanical materials are listed in Table 1.

B. Temperature Comparison of the Analytical Simulation

Figure 6 gives the temperature comparison between the experimental and analytical results. The solid line represents the analytical temperature at radial positions from the very center to the edge on the top surface of the lens element while the red dots are values of the thermal sensors. As can be seen, the temperature differences are 0.170°C ± 0.01°C, −0.042°C ± 0.01°C, and −0.024°C ± 0.01°C, considering the accuracy of the temperature sensor, at different spots. The temperature at the edge of the lens element rises to 22.51°C, which is enough for the experiment.

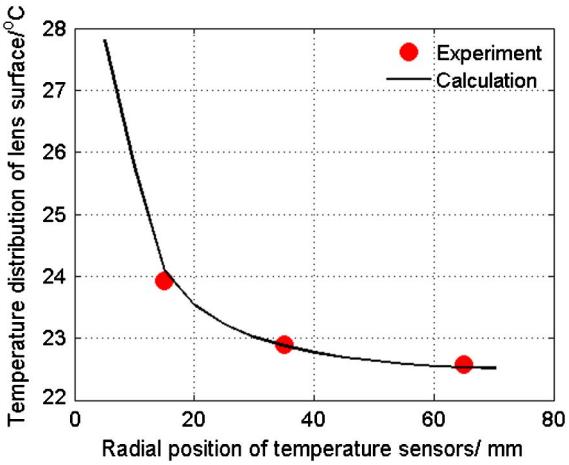

Fig. 6. Comparison of temperature between experiment and simulation.

C. Analysis and Comparison of Experiment and Simulation

Experimental and analytical top-surface figures of the lens element are shown in Fig. 7. The first picture of the measured result has three dark parts without testing data because the electrical film heater, the cables of the electrical film heater, and the thermal sensor block the measuring light of the interferometer. To eliminate the effects of the cables, the simulated result is disposed in the same way. As can be seen, the experimental surface figure is 9.622 nm RMS while the simulated result is 8.097 nm RMS.

The fringe Zernike coefficients and the differences between experiment and simulation are shown in Fig. 8. The main components are axially symmetrical terms, like Z4, Z9, and Z16, which is mainly due to the central location of the film heater.

Figure 9 compares the results of transmission WFE between experiment and numerical analysis due to the electrical film heater. The transmission WFEs are similar, and the numerical value is relatively larger than the experiment.

The Zernike coefficients comparison of transmission WFE and the differences of each term are listed in Fig. 10. The defocus and spherical terms occupy the most part of the transmission WFE and are even bigger than the value of every term of the top surface figure. In Fig. 8, the numerical temperature in the center of the lens element is larger than the experimental result, which is consistent with the Zernike coefficient distribution in Fig. 9. However, it is different for the surface figure result, which should have the same trend as the transmission WFE. The environmental instability, the boundary condition

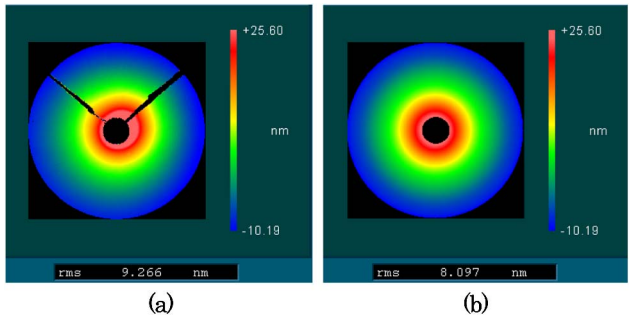

Fig. 7. Surface figure from experiment and numerical simulation. (a) Surface figure from experiment. (b) Surface figure from numerical simulation.

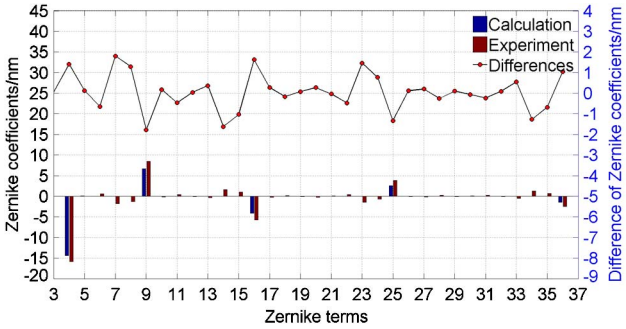

Fig. 8. Fringe Zernike coefficients distribution of tested and simulation surface figure and difference between them.

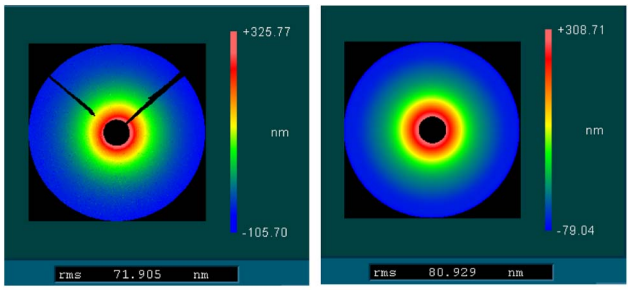

Fig. 9. Surface figure from experiment and numerical simulation. (a) Wavefront from experiment. (b) Wavefront from numerical simulation.

difference, and the different measuring principles between the surface figure and the transmission WFE could account for the above phenomenon.

In order to evaluate the magnitude of trefoil aberration, which might be caused by the three main supporting legs of the kinematic mounting, coefficients of trefoil and the corresponding RMS value contained in the surface figure and WFE acquired by experiment and simulation have been listed in Table 2. The equivalent magnitude forms as Magnitude $= (A_{mn}^2 + B_{mn}^2)^{1/2}$, in which A_{mn} and B_{mn} are the corresponding coefficients in Eq. (3).

As we can see, the coefficients and RMS values in the experiment are relatively bigger than those in the simulation. Actually, the proportions of RMS value of trefoil to total surface figure and WFE RMS value from experiment are very small, only

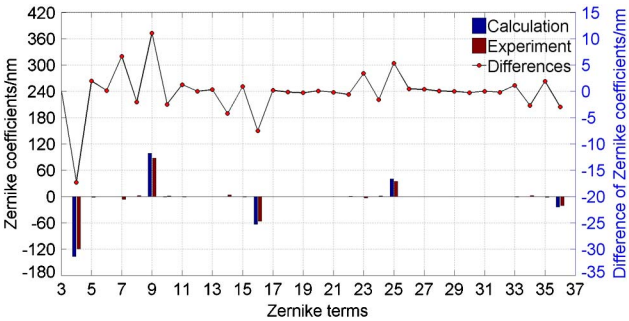

Fig. 10. Fringe Zernike coefficient distribution of tested and simulation wavefront and the difference between them.

Table 2. RMS Value of Pre Trefoil of Surface Figure and Wavefront from Experiment Measurements and Simulation (unit:nm)

	Experiments		Numerical Simulation	
	Coefficients	RMS	Coefficients	RMS
Surface	0.510	0.180	0.026	0.010
Wavefront	1.976	0.699	0.980	0.346

counting for 0.97% and 1.94%, respectively. This asymmetrical aberration might be the result of nonuniformity of the thermal load or centration error of the heater. From Table 2 it is obvious that the trefoil aberration is negligibly small so that it is hard to make a distinction whether it is caused by the experimental disturbance or by the kinematic mounting. In fact, the thermal loads applied in the experiments are much bigger than the actual heat absorbed in the projection lens. So the trefoil aberration in every lens element would be even smaller inside the projection lens in situation.

6. Conclusion

This paper focuses on the thermal–optical characteristics of the basic lens cell with a kinematic mounting. According to the simulation and experimental results, the specified heat load leads to a temperature rise of 22.51°C at the edge and a radial gradient of 5.3°C on the top surface of the lens element. The dominating aberrations are axially symmetrical terms, like Z4, Z9, and Z16. The experiments and simulation have shown the same results. In this case, RMS values of first-order trefoil aberration are observed and account for less than 1% and 2% of the total WFE and the surface figure of the lens element, respectively, which are negligible compared to Z4, Z9, and Z16. In the experiments, it is hard to control the centration location and the heat uniformity of the heater, which causes the differences between experiment and simulation. However, these differences are reasonable and have no decisive influence on the final evaluation of the lens cell. Therefore, the proper radial flexibility of the main supporting legs has been proved, and the kinematic mounting turns out to have good thermal adaptability in the application of a projection lens. This study of the thermal-optical characteristics of the basic lens cell has set up a theoretical and experimental basis for the prediction of the thermal aberration of the projection lens. This method could also be applied in other precision optomechanical systems.

References

1. T. Nakashima, Y. Ohmura, T. Ogata, Y. Uehara, H. Nishinaga, and T. Matsuyama, "Thermal aberration control in projection lens," Proc. SPIE **6924**, 69241 (2008).
2. Y. Uehara, T. Matsuyama, T. Nakashima, Y. Ohmura, T. Ogata, K. Suzuki, and N. Tokuda, "Thermal aberration control for low k1 lithography," Proc. SPIE **6520**, 65202V (2007).
3. Y. Ohmura, T. Ogata, T. Hirayama, H. Nishinaga, T. Shiota, S. Ishiyama, S. Isago, H. Kawahara, and T. Matsuyama, "An aberration control of projection optics for multi-patterning lithography," Proc. SPIE **7973**, 79730 (2011).

4. T. Yoshihara, T. Sukegawa, N. Yabu, M. Kobayashi, T. Arai, T. Kitamura, A. Shigenobu, Y. Hasegawa, and K. Takahashi, "Advanced aberration control in projection optics for double patterning," Proc. SPIE **7274**, 72741 (2009).
5. H. Chen, H. Yang, X. Yu, and Z. Shi, "Simulated and experimental study of laser-beam induced thermal aberrations in precision optical systems," Appl. Opt. **52**, 4370–4376 (2013).
6. P. R. Yoder, *Opto-Mechanical Systems Design* (Academic, 2006).
7. Z. Wang, Y. Zhai, G. Mei, F. Jiang, and Z. Cheng, "Design of flexible support structure of reflector in space remote sensor," Opt. Precision Eng. **18**, 1833–1841 (2011).
8. R. Fata, V. Kradinov, and D. Fabricant, "Flexure mounts for high performance astronomical lenses: ground-based and airborne instrumentation for astronomy," Proc. SPIE **6269**, 62695 (2006).
9. H.-S. Yang, H. Kihm, I. K. Moon, G.-J. Jung, S.-C. Choi, K.-J. Lee, H.-Y. Hwang, S.-W. Kim, and Y.-W. Lee, "Three-shell based lens barrel for the effective athermalization of an IR optical system," Appl. Opt. **50**, 6206–6213 (2011).
10. F. Staals, A. Andryzhyieuskaya, H. Bakker, M. Beems, J. Finders, T. Hollink, J. Mulkens, A. Nachtwein, and R. Willekers, "Advanced wavefront engineering for improved imaging and overlay applications on a 1.35 NA immersion scanner," Proc. SPIE **7973**, 79731 (2011).
11. C. Evans, *Precision Engineering: An Evolutionary View* (Academic, 1989).
12. A. H. Slocum, "Kinematics couplings: a review of design principles and application," Int. J. Mach. Tools Manuf. **50**, 310–327 (2010).
13. M. L. Culpepper, M. V. Kartik, and C. Dibiasio, "Design of integrated eccentric mechanisms and exact constraint fixtures for micro-level repeatability and accuracy," Precis. Eng. **29**, 65–80 (2005).
14. SigFit Reference Manual, version 2012R1d, Sigmadyne Inc.